Frequency-resolved interferometer measurements of polarized wave propagation in scattering media

Timothy D. Gerke, Mark A. Webster, Andrew M. Weiner, and Kevin J. Webb

School of Electrical and Computer Engineering, Purdue University, 465 Northwestern Avenue, West Lafayette, Indiana 47907-2035

Received January 26, 2005; accepted April 7, 2005

An interferometric technique is utilized to measure both the time- and frequency-domain optical fields scattered by a random medium. The method uses a tunable continuous-wave laser source to make frequency-resolved measurements within a fixed-path-length interferometer. Measured frequency-domain field statistics, with a linearly polarized input, are shown to be zero-mean, circular complex Gaussian for both co- and cross-polarization states. With decreasing scatter, the extracted average impulse responses for co- and cross-polarized states show distinct differences, thereby providing insight into the scattering domain. © 2005 Optical Society of America

OCIS codes: 030.6140, 030.6600, 120.3180, 290.4210, 290.7050.

1. INTRODUCTION

Understanding the effects of scattering in wave propagation is important for the characterization and imaging of turbid media. Specific applications of such work are extremely broad and include atmospheric and environmental sensing,[1] optical-fiber characterization,[2] and biomedical imaging.[3–6] Techniques for optical imaging, in particular, have been developed using both coherent and incoherent light. For example, the interference of low coherence, reflected light is utilized for imaging weakly scattering media in optical coherence tomography,[3] and *in vivo* three-dimensional imaging has been achieved with very high resolution into a few millimeters of tissue.[4] Optical diffusion tomography has also become an established method for three-dimensional imaging that utilizes incoherent light with a diffusion-equation forward model to determine properties of a more strongly scattering medium, and this approach can be used for *in vivo* imaging.[5,6] Neither of these methods, however, utilizes the information available in the speckle patterns that result from scattered, coherent light.

Much has been done to extract useful information from speckle patterns with the goal of imaging or characterization of scattering media. In 1970, for example, Labeyrie[7] demonstrated that Fourier analysis of speckle patterns could be used to increase the resolution of deep-space images to very nearly the diffraction limit. Creath[8] and Leendertz[9] showed that correlations of double-exposure speckle patterns provide information remotely about deformations of the surface of a reflector that could be used to compute stress or strain on the surface. Thompson *et al.*[10,11] measured the speckle contrast ratio as a function of sample thickness using light of fixed coherence and applied a diffusion-equation model to compute the scattering coefficient. McKinney *et al.*[12] used the contrast ratio as a function of source coherence—achieved using a frequency-scanned, external-cavity laser diode with a scan time short relative to the detector integration time—to extract the scattering properties, again with the aid of a diffusion model. Using this approach and appropriate coherence, inhomogeneities in scattering properties have been detected.[12] Such measurements with a diffusion-equation model can be used to generate a photon time-of-flight or path-length distribution, i.e., the normalized temporal Green's function. Third-order frequency correlations of speckle patterns have been shown to provide photon time-of-flight distribution without recourse to a model by Webster *et al.*[13,14] under the assumption of zero-mean, circular complex Gaussian fields.

Interferometer measurements of the random intensity of a single speckle spot have been used to compute the temporal response of a scattering medium. Tualle *et al.*[15] used an experimental configuration, sinusoidally modulated the source frequency, and mathematically used a "coherence gate" to select light delayed relative to the reference arm by a variable amount. The result was a direct measure of the temporal response of a random medium using an intensity-based measurement.

In the microwave region, randomly filled waveguides have been studied by Chabanov and Genack[16] and Sebbah *et al.*[17,18] The use of a wire-probe antenna as the detector enables direct measurement of the electric field and the study of its statistics, which were shown to be circular Gaussian with a nonzero mean.[16–18] Pearce *et al.*[19] have provided evidence of zero-mean, circular complex Gaussian fields from a terahertz time-domain spectroscopy measurement. Their results showed some deviation from circular Gaussian, attributable to a nonuniform power spectrum over the bandwidth utilized due to the finite temporal width of the input pulse. Using an interferometric technique, we have previously measured the complex field amplitude at optical frequencies, and shown it to

1084-7529/05/122691-9/$15.00

agree well with the presumption (see Goodman[20]) that the statistics of the field scattered by a coherently illuminated, random medium are zero-mean, circular Gaussian over better than three orders of magnitude.[21]

Polarization-based measurements of scattered fields have the potential to communicate more information regarding scatterer properties than conventional single-polarization-state measurements. From short pulse measurements, Ito and Oguchi[22] and Ishimaru *et al.*[23] have found the degree of polarization as a function of material thickness and particle size for both linearly and circularly polarized inputs. This suggests a polarization-dependent temporal response that has indeed been obtained from the Stokes vector by Wang *et al.*[24] Monte Carlo simulations of the temporal responses for the total intensity (the first Stokes parameter) and the difference between the co- and cross-polarized states (second Stokes parameter) agreed well with data measured using a 100 fs pulsed source and a streak camera detector. Interestingly, the co-polarized response was found to be larger than the cross-polarized result for short times, and the two responses were similar for later times.

Here we establish a technique using spectral interferometry that has found wide application—including spectroscopy[25] and fiber characterization[2]—to provide insight into the scattering domain by measuring the complex electric field amplitude, and consequently the temporal response, of the co- and cross-polarization states of a scattering medium with a linearly polarized input. In this interferometer configuration, an inverse Fourier transform (IFT), shift and selective window, and Fourier transform (FT) of the measured intensity data yield the electric field magnitude and phase. The normalized ensemble-average temporal response, denoted by $p(t)$, is found directly from the computed frequency-domain field amplitude and is the probability-density function for the time-of-flight of the scattered partial waves traversing the medium.

We use our interferometer technique to measure the scattered field amplitude in the co- and cross-polarization states and verify that the fields are zero-mean, circular complex Gaussian. We also provide a measure of the evolution of the degree of polarization with material thickness that relates to the number of scattering events. With that information, we proceed to compute the normalized temporal response for both the co- and cross-polarization states as well as the total (the sum of the intensities in the two orthogonal linear polarization states) temporal response. We show distinct differences in the co-polarized and cross-polarized temporal responses for weaker scatter, and reveal that they approach one another as the scatter increases.

2. THEORY

A. Scattered Field

At a particular point in space, the field scattered by a random medium is the superposition of the many scattered partial waves that propagate through the medium by different paths. Assuming a scalar model, the resultant field $e_{\text{out}}(t', \nu)$ can be described by

$$e_{\text{out}}(t', \nu) = E_o(\nu)\exp[j2\pi(\nu_o + \nu)t'] + \text{c.c.}, \tag{1}$$

where ν_o is the center frequency of the tunable input, $E_o(\nu)$ is the complex electric field amplitude due to an input with a frequency $\nu_o + \nu$, and c.c. represents the complex conjugate.[14] We have used t' to denote the laboratory time variable, while ν is used to denote the source frequency-tuning variable and has a Fourier conjugate variable t.

Scattering events contribute to the depolarization of a polarized input.[23] Therefore, using a vector description for the resultant output field, we assume the Cartesian form

$$\mathbf{e}_{\text{out}}(t', \nu) = \hat{\mathbf{x}}E_{\parallel}(\nu)\exp[j2\pi(\nu_o + \nu)t'] + \hat{\mathbf{y}}E_{\perp}(\nu)\exp[j2\pi(\nu_o + \nu)t'] + \text{c.c.}, \tag{2}$$

in the case of an input field linearly polarized in the $\hat{\mathbf{x}}$ direction. The portion of the scattered field that is polarized in the same direction as the input is defined as the co-polarized field and is denoted by a subscript $\parallel$; that polarized in the orthogonal direction is defined as the cross-polarized field and is denoted by a subscript $\perp$.

B. Field Measurement Using Spectral Interferometry

Consider the experimental setup shown in Fig. 1. The source is a single-mode continuous-wave (CW) tunable laser diode with high coherence. The measurement consists of modulating the source frequency, $\nu_o + \nu$, and recording the intensity output of the interferometer with a photodetector that has an aperture that is small relative to the speckle correlation size. The input field to the interferometer $\mathbf{e}_{\text{in}}(t')$ is assumed to have the form

$$\mathbf{e}_{\text{in}}(t') = \hat{\mathbf{x}}E_{\text{in}}\exp[j2\pi(\nu_o + \nu)t'] + \text{c.c.} \tag{3}$$

In the reference arm of the interferometer, the attenuator is a half-wave plate (HWP) and linear polarizer (LP) combination that can rotate the state of linear polariza-

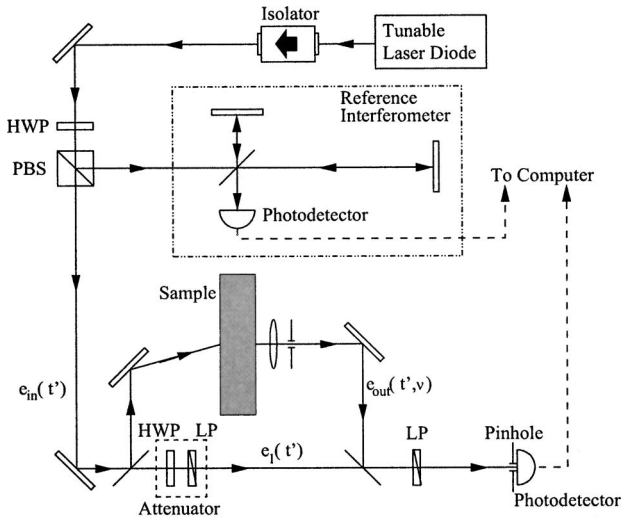

Fig. 1. Experimental setup; HWP is a half-wave plate, LP is a linear polarizer, PBS is a polarizing beam splitting cube, and the attenuator is composed of a HWP-LP pair.

tion and attenuate the field intensity. The field in the reference arm of the interferometer after the attenuator is given by

$$\mathbf{e}_1(t') = \hat{\mathbf{p}} E_1 \exp[j2\pi(\nu_o + \nu)t'] + \text{c.c.}, \tag{4}$$

where $\hat{\mathbf{p}}$ denotes the orientation of the polarizer in the attenuator combination and E_1 is the field amplitude. Similarly, the field in the sample arm of the interferometer after passing through the random medium is given by

$$\mathbf{e}_{\text{out}}(t', \nu) = \hat{\mathbf{x}} E_{\parallel}(\nu)\exp[j2\pi(\nu_o + \nu)(t' - \tau)] + \hat{\mathbf{y}} E_{\perp}(\nu)\exp[j2\pi(\nu_o + \nu)(t' - \tau)] + \text{c.c.}, \tag{5}$$

where $\tau = \Delta L/c$ is the interferometer characteristic time delay for an optical-path-length difference between the two interferometer arms of ΔL and c is the speed of light in a vacuum.

The total output field from the interferometer is given by the superposition of the fields of Eqs. (4) and (5). When the polarizer in front of the photodetector is oriented in the $\hat{\mathbf{x}}$ direction and $\hat{\mathbf{p}} = \hat{\mathbf{x}}$, the detected intensity is determined from the total field complex amplitude (ignoring unit-based constants) by

$$\begin{aligned} I(\nu) &= |E_1 + E_{\parallel}(\nu)\exp[-j2\pi(\nu_o + \nu)\tau]|^2 \\ &= |E_1|^2 + |E_{\parallel}(\nu)|^2 + E_1^* E_{\parallel}(\nu)\exp[-j2\pi\nu\tau] \\ &\quad + E_1 E_{\parallel}^*(\nu)\exp[j2\pi\nu\tau], \end{aligned} \tag{6}$$

where the arbitrary constant phase term $\exp(j2\pi\nu_o\tau)$ has been dropped. From Eq. (6) we see that the measured intensity from the interferometer is dependent on the copolarized scattered field, $E_{\parallel}(\nu)$. By setting $\hat{\mathbf{p}} = \hat{\mathbf{y}}$ in Eq. (4) and orienting the polarizer in front of the photodetector to the $\hat{\mathbf{y}}$-direction, we can measure an output intensity that is dependent on the cross-polarized field, $E_{\perp}(\nu)$. For notational convenience, we shall use $E(\nu)$ to represent either $E_{\parallel}(\nu)$ or $E_{\perp}(\nu)$ in the subsequent derivations. Also, without loss of generality, we can set the arbitrary constant of E_1 to unity.

Taking the IFT of Eq. (6), giving $i(t) = \int_{-\infty}^{\infty} I(\nu)\exp(j2\pi\nu t)\mathrm{d}\nu$, provides some insight into the information carried within the detected signal. Consider

$$i(t) = \delta(t) + g(t) + e(t - \tau) + e^*(-t - \tau), \tag{7}$$

where $g(t)$ and $e(t)$ are defined as the IFTs of $|E(\nu)|^2$ and $E(\nu)$, respectively, and $\delta(t)$ is the Dirac delta function. It is apparent that the first two terms in Eq. (7) are centered about $t = 0$, while the third and fourth terms are time-shifted to $t = \pm\tau$, as pictured in Fig. 2. The time-shifted components are those of most interest because they contain information about the complex random field. The same information can be extracted from either, but we choose the third term for simplicity, since it deals with $E(\nu)$ rather than its complex conjugate. Choosing τ such that the two time-shifted components of Eq. (7) do not overlap with those centered at the origin separates these terms and allows them to be analyzed. It is important to note that $e(t)$, which is the field impulse response function for a single-scatterer configuration, will be approximately zero for all $t < 0$ when the measurement is performed with sufficient bandwidth and, as will be shown later, it is directly related to the temporal response, which is a causal function. Thus, the features of the third term can be separated from the other features in Eq. (7) with a temporal windowing function, giving

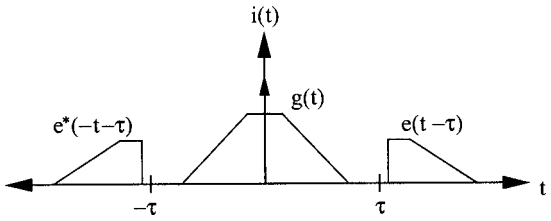

Fig. 2. Example of the temporal features of $i(t)$.

$$e(t - \tau) = i(t)u(t - \tau + \delta), \tag{8}$$

where $u(t)$ is a unit step function and δ is a small positive offset to allow for the smoothing influence of the finite measurement bandwidth. The frequency-domain complex field amplitude $E(\nu)$ is determined by time-shifting Eq. (8) by $+\tau$, then taking a FT, giving

$$E(\nu) = \int_{-\infty}^{\infty} i(t + \tau)u(t + \delta)\exp(-j2\pi\nu t)\mathrm{d}t. \tag{9}$$

In summary, the steps necessary to compute the random field complex amplitude are: (i) IFT the measured frequency-domain intensity data of Eq. (6), (ii) selectively window the data of Eq. (7) to give the expression of Eq. (8), (iii) time-shift the windowed data by $+\tau$, and (iv) FT this result to the frequency domain, which yields the result of Eq. (9), the frequency-domain scattered complex field amplitude.

C. Temporal Intensity Impulse Response

We estimate the ensemble-average intensity impulse response by using data from N sample positions. For convenience, we define a normalized temporal response for the nth sample as

$$p_n(t) = \frac{|e(t)|^2}{\langle I\rangle_t} = \frac{|i(t + \tau)u(t + \delta)|^2}{\langle I\rangle_t}, \tag{10}$$

where $\langle I\rangle_t = \int_{-\infty}^{\infty}|e(t)|^2\mathrm{d}t$ and $p_n(t)$ may represent either $p_{n\parallel}(t)$ or $p_{n\perp}(t)$ accordingly with $E_{\parallel}(\nu)$ or $E_{\perp}(\nu)$. Using Eq. (10), the ensemble average of the measurements for many configurations of scatterers, with spatial average $\langle p_n(t)\rangle_s \equiv p(t)$, where $\langle\cdot\rangle$ is the spatial average, is

$$p(t) = \frac{1}{N}\sum_{n=1}^{N} p_n(t). \tag{11}$$

A finite measurement bandwidth B results in a temporal feature resolution $\sim 1/B$. The shift in the temporal window $u(t + \delta)$ was to allow for this near $t = \tau$. More generally, the finite bandwidth is equivalent to multiplying the ideal, infinite bandwidth field amplitude $E_{\infty}(\nu)$ by a rectangular windowing function $W_{\text{R}}(\nu)$, whereby Eq. (9) becomes

$$E(\nu) = E_{\infty}(\nu) W_{\mathrm{R}}(\nu) = \int_{-\infty}^{\infty} i(t+\tau) u(t+\delta) \exp(-j2\pi\nu t) \mathrm{d}t, \qquad (12)$$

with $i(t)$ being the IFT of the bandwidth-limited measured data and $E(\nu)$ the band-limited scattered complex field amplitude.

3. EXPERIMENT

The experimental setup that was used for our measurements is shown in Fig. 1. The scattering samples were composed of a clear acrylic that was cast with a homogeneous suspension of 50 nm TiO_2 particles (Cyro Industries, Acrylite FF). The reduced scattering coefficients in a diffusion model ($\mu_s' \simeq 1/l_s$, where l_s is the mean free path,[26] the distance for the photon direction to become randomized) for the two samples studied were $\mu_s' = 4\ \mathrm{cm}^{-1}$ and $14\ \mathrm{cm}^{-1}$.

The laser source we used was an external-cavity, tunable laser diode (New Focus Vortex 6017). The nominal linewidth of this laser system gives a coherence length of around 60 m. The experiment requires the coherence length be greater than the interferometer path-length difference (including that due to the scattering sample), so that the beams interfere efficiently. The laser has a center wavelength of approximately 850 nm (353 THz) and can be scanned over approximately 80 GHz. The frequency tuning was performed by applying a voltage to a piezoelectric transducer, upon which is mounted one of the cavity mirrors. For this purpose, a 1 Hz, 4 V peak-to-peak triangle wave was used while ensuring interferometer stability during the data acquisition time. Only 60 GHz of the measured bandwidth was used in order to avoid transition effects of the abrupt modulation changes due to the triangular modulation waveform peaks.

Referring to Fig. 1, the source was split into two beams with a polarizing beam splitter for use with the two interferometer configurations. The relative powers of the split beams were controlled by the HWP and polarizing beam splitter. The reference interferometer was constructed in a Michelson configuration (seen in Fig. 1) and was used to provide a measure of the frequency of each data point throughout the frequency scan. For accurate frequency measurement, the optical-path-length difference ($\sim$4 m) of the two arms was approximately four times greater than that of the sample interferometer. The intensity signal from the reference interferometer was monitored with a silicon p-i-n diode (Thorlabs DET201) photodetector.

The sample interferometer is the Mach–Zehnder interferometer seen in Fig. 1. The beam at the front face of the scattering sample was incident at an angle of approximately 5° from normal so that for weakly scattering samples, ballistic light was reduced. From Eqs. (8) and (9), it is apparent that the interferometer time offset, τ, must be known in order to have a correct time reference for the time-domain field impulse response $e(t)$. The time offset, due to the effective path-length difference between the two arms of the interferometer, was found by making a measurement of a clear sample with a rough surface, which was necessary because of the nonnormal incidence of the input. In this case, Eq. (7) will ideally comprise delta functions at $t=0$ and $t=\pm\tau$, where τ includes a nonscattering sample delay time $t_s=(n-1)d/c$, with n the index of refraction and d the clear sample thickness. The value for τ can be found from the peak of the short pulses having positive or negative temporal offset. The ability to obtain the exact time reference is one of the important traits of the interferometer measurement, whereas, for example, a third-order intensity correlation measurement of the temporal impulse[13,14] is insensitive to time offset.

Figure 1 shows the sample in the longer arm of the interferometer. In this arrangement, the temporal field impulse response starts at $\pm\tau$ and trails away from the origin. Placing the sample in the shorter arm causes the placement of the offset temporal field impulse and its complex conjugate in Eq. (7) to be inverted, and thus they begin at $\pm\tau$ and trail inward. This could cause aliasing so this configuration was avoided.

The detector for the sample interferometer, which was used to monitor the signal corresponding to Eq. (6), was an amplified p-i-n diode (New Focus 2001). The detector contains a variable gain amplifier and bandpass filter that allows for measurement of only the relevant signal. With a frequency scan over the total bandwidth of 80 GHz in a time of 0.5 s used in the experiment, given the interferometer delay of $\tau=3.3$ ns, the carrier frequency for the detected signal is $f_c' = 80\ \mathrm{GHz} \times 3.3\ \mathrm{ns}/0.5\ \mathrm{s} = 528$ Hz. We used a detector bandpass filter of 300 Hz to 10 kHz. This aids in reducing the signal associated with the first two terms in Eq. (6).

To extract information about the scattering medium from the scattered field, it is important that the detector aperture be small relative to the speckle spatial correlation size, which is a measure of the speckle spot size. Therefore, an appropriate imaging system consisting of an imaging lens and limiting aperture pair was designed to make the projected spot size significantly larger than the detection area at the detector plane, which was a circular aperture with a radius of 0.5 mm. The lens imaged the light scattered by the sample to the detector plane, while the limiting aperture controlled the speckle feature size. The feature size can be approximated by the Airy pattern, which provides that 84% of the light passing through a small circular aperture is concentrated about a central ring of radius $r=1.22\lambda z_i/D$, where z_i is the image distance and D is the diameter of the aperture.[27] We used a lens with a focal length of 50 mm, an aperture of radius 1 mm, and an image distance of 2 m, which created imaged speckle spots of 2 mm average radius. So, to formulate good ensemble statistics from statistically independent data, the sample was translated 500 μm perpendicular to beam propagation between measurements, which corresponded to a translation in the detector plane of approximately 20 mm due to the magnification factor of approximately 40 for our imaging configuration.

The sample and reference interferometer detector signals were recorded using a personal computer with data acquisition capabilities. The acquisition process was controlled with a program written using data acquisition software that recorded the frequency modulating waveform and the signals from the detectors for each interfer-

ometer. Using the frequency modulating waveform, data from a single frequency scan were extracted from the measurement results. The reference interferometer signal was then used to compute the frequency at each data point, and, finally, the sample interferometer data were processed according to the steps outlined in Section 2 with $\delta=0.5$ ns (refer to Eq. (8)) using numerical software routines.

4. EXPERIMENTAL RESULTS

A. Measured Fields

The procedure of subsection 2.B was used to extract random field samples as a function of time and frequency. Figure 3 shows an example result for the IFT of measured co-polarized data. The real part of $i(t)$ is shown for a single sample position for a sample having $\mu_s'=14$ cm^{-1} and a thickness of 12 mm. The features, $g(t)$, $e(t-\tau)$, and $e^*(-t-\tau)$, where $\tau=3.3$ ns, can be observed. The feature beginning at a delayed time of approximately 3.3 ns is the data that are windowed and IFTed to yield $E(\nu)$. The spikes at 2 ns and 5.3 ns are likely due to extraneous reflections in the interferometer.

Results for the co-polarized $e(t)$ for four measurement positions of the 12 mm sample of the $\mu_s'=4$ cm^{-1} material are shown in Fig. 4(a), along with the real part of the FT of these data in Fig. 4(b). The data in these figures have been offset for clarity.

B. Field Statistics

Although it is not required by our method, we demonstrate that the field scattered by a turbid medium is described by zero-mean, circular complex Gaussian statistics. We have previously conducted field measurements and provided evidence for zero-mean, circular Gaussian statistics with our frequency-resolved technique for samples that completely depolarize the linearly polarized input.[21] Here we extend those results to samples that do not completely depolarize the input and we find that both the co-polarized and cross-polarized fields are also well described by zero-mean, circular Gaussian statistics. Figure 5 shows the statistics of the measured co- and cross-polarized frequency-domain scattered fields for the 9 mm sample having $\mu_s'=4$ cm^{-1}, obtained using 100 independent measurements of the frequency-domain complex field amplitude, as expressed in Eq. (9). Good agreement with a Gaussian curve is apparent and was observed for all samples tested for both polarization states. When the degree of polarization [DOP, or P; see Eq. (17)] is nonzero,

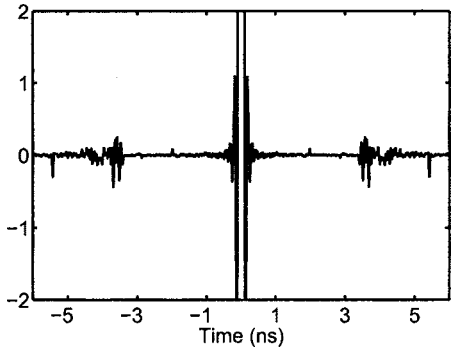

Fig. 3. Example of the real part of the measured temporal features of the co-polarized $i(t)$ for a 12 mm sample with $\mu_s'=14$ cm^{-1} and $\tau=3.3$ ns.

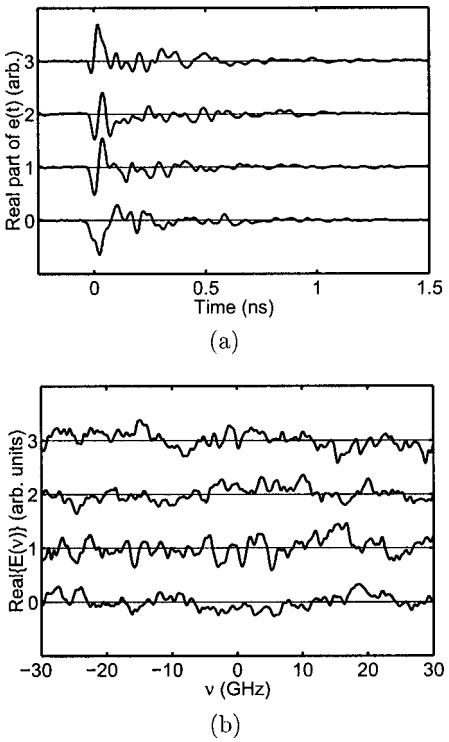

Fig. 4. Real parts of four individual measurements of the (a) time, (b) frequency-domain scattered fields, offset for clarity. The sample has $\mu_s'=4$ cm^{-1} and a thickness of 12 mm. These data are for co-polarized light.

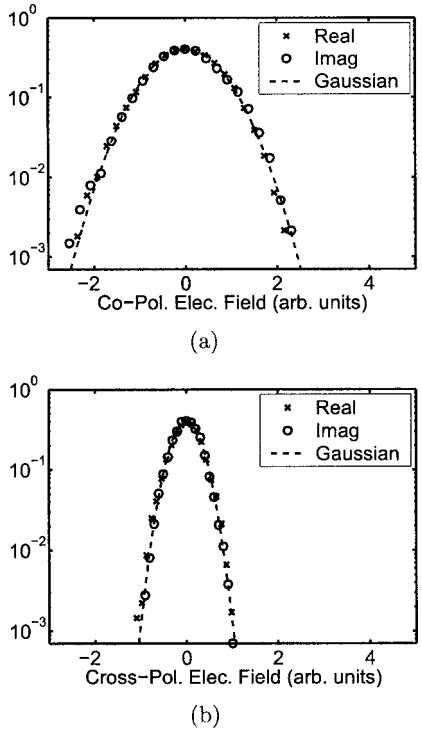

Fig. 5. Measured probability distribution for (a) co-polarized, (b) cross-polarized frequency-domain scattered fields for a 9 mm sample ($\mu_s'=4$ cm^{-1}). For this sample, the DOP is $P=0.4$.

as is the case for Fig. 5, to maximize the experimental dynamic range we attenuated the input field by different amounts for the co-polarized and cross-polarized measurements. Therefore, to directly compare the measured statistics for each polarization state, we normalized the average intensity of each measurement to unity then multiplied by factors of $\frac{1}{2}[1+P]$ and $\frac{1}{2}[1-P]$ for co- and cross-polarization states, respectively.

C. Temporal Resolution and Autocorrelations

We consider field and intensity autocorrelations of measured data. In order to prevent ripple from the finite measurement bandwidth camouflaging the underlying features, we apply a Hamming window,[28] giving

$$e_{\mathrm{H}}(t) = e(t) * w_{\mathrm{H}}(t) = \int_{-\infty}^{\infty} E(\nu) W_{\mathrm{H}}(\nu) \exp(j2\pi\nu t) \mathrm{d}\nu, \tag{13}$$

where $e_{\mathrm{H}}(t)$ is the windowed result and $e(t)$ is the measured data. The computed temporal response is then a function of the measured temporal field response convolved with the pulse $w_{\mathrm{H}}(t)$:

$$p_{nH}(t) = \frac{|e_{\mathrm{H}}(t)|^2}{\langle I \rangle_t} = \frac{|e(t) * w_{\mathrm{H}}(t)|^2}{\langle I \rangle_t}, \tag{14}$$

where $*$ is the convolution operator. As evident in Eq. (14), the temporal resolution of $e_H(t)$ is dictated by the width of $w_{\mathrm{H}}(t)$.

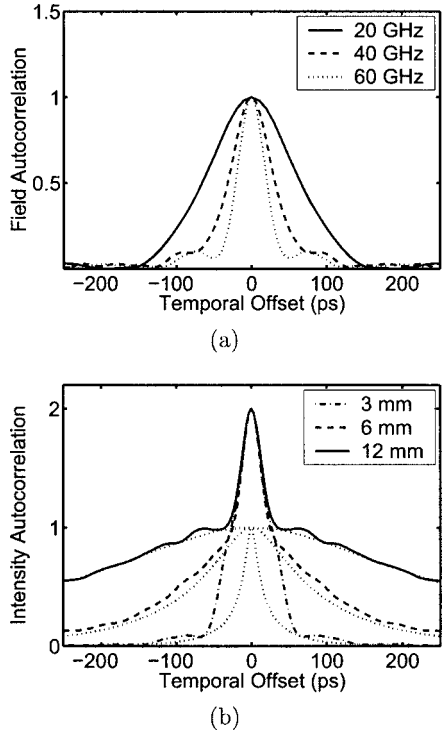

Fig. 6. (a) Field autocorrelation peak (6 mm sample only) for co-polarized light and bandwidths of 60, 40, 20 GHz. (b) Total intensity (co-polarized plus cross-polarized light) autocorrelation for 3, 6, 12 mm thick samples of $\mu_s' = 14\ \mathrm{cm}^{-1}$, averaged over 100 measurements with a bandwidth of 60 GHz, and with the autocorrelation of the diffusion model simulated results overlaid in dotted curves.

The field and intensity temporal autocorrelations provide information on the temporal characteristics of the scattered field, subject to this temporal resolution. The field autocorrelation is

$$G_1(\eta) = \left\langle \int_{-\infty}^{\infty} e_{\mathrm{H}}(t+\eta) e_{\mathrm{H}}^*(t) \mathrm{d}t \right\rangle_s, \tag{15}$$

where $e_{\mathrm{H}}(t)$ is an individual Hamming-windowed, band-limited measurement of the temporal field impulse response and $\langle \cdot \rangle_s$ is an ensemble average over space. The intensity autocorrelation is

$$G_2(\eta) = \left\langle \int_{-\infty}^{\infty} p_n(t+\eta) p_n(t) \mathrm{d}t \right\rangle_s, \tag{16}$$

where $p_n(t) = |e_{\mathrm{H}}(t)|^2 / \langle I \rangle_t$ is the temporal intensity impulse response for the nth configuration of scatterers.

Figure 6(a) shows the field correlation $G_1(\eta)$ for co-polarized light and Fig. 6(b) shows the total intensity (co-polarized plus cross-polarized light) correlation for data obtained by averaging over 100 measurement positions for 3, 6, and 12 mm samples having $\mu_s' = 14\ \mathrm{cm}^{-1}$. The average field correlation is nearly zero except in the neighborhood of the correlation peak at $\eta = 0$. The half width at half maximum of the field autocorrelation peaks for measurement bandwidths of 20, 40, and 60 GHz, from Fig. 6(a), with a Hamming window, are approximately 66, 33, and 21 ps, respectively. Figure 6(b) shows a comparison between the measured intensity autocorrelation and that obtained using a diffusion-equation model. The intensity autocorrelation data comprises a peak atop a pedestal. The peak is associated with the finite measurement bandwidth and the pedestal with the duration of $p(t)$. Such responses are well known in the field of ultrafast optics.[29] For the 6 and 12 mm samples, where the intensity autocorrelation is wider than the correlation peak, the agreement with a diffusion model for larger $|\eta|$ is good.

D. Polarized Temporal Response

The method by which the co-polarized and cross-polarized temporal responses are normalized is as follows. A measure of the DOP (or P), which gives the energy contained in one state relative to the other, of the sample in question is required. We define P as

$$P = \frac{\langle I_{\parallel} \rangle_s - \langle I_{\perp} \rangle_s}{\langle I_{\parallel} \rangle_s + \langle I_{\perp} \rangle_s}, \tag{17}$$

where $\langle \cdot \rangle_s$ is a spatial average using data from different sample positions, and $\langle I_{\parallel} \rangle_s$ and $\langle I_{\perp} \rangle_s$ are the co- and cross-polarized spatial mean intensities, respectively. $\langle I_{\parallel} \rangle_s$ and $\langle I_{\perp} \rangle_s$ were measured as the average scattered intensity in each polarization state using a linear polarizer to select the polarization and a converging lens to focus a large portion of the resulting speckle pattern to the face of the amplified p-i-n diode. Once P is known, each temporal response is normalized to unity and multiplied by a factor ($\frac{1}{2}[1+P]$ and $\frac{1}{2}[1-P]$ for co-polarized and cross-polarization states, respectively), such that the relative energies of the two responses agree with the DOP measurement. This also provides that the sum of the co- and

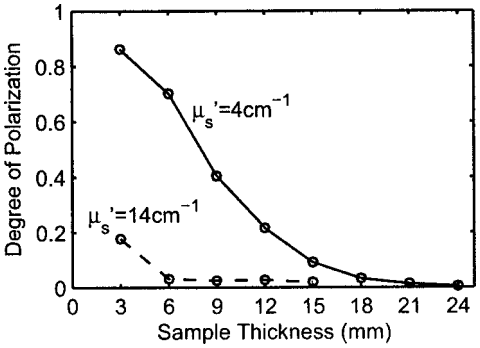

Fig. 7. Degree of polarization plotted as a function of sample thickness for two samples with differing reduced scattering coefficients.

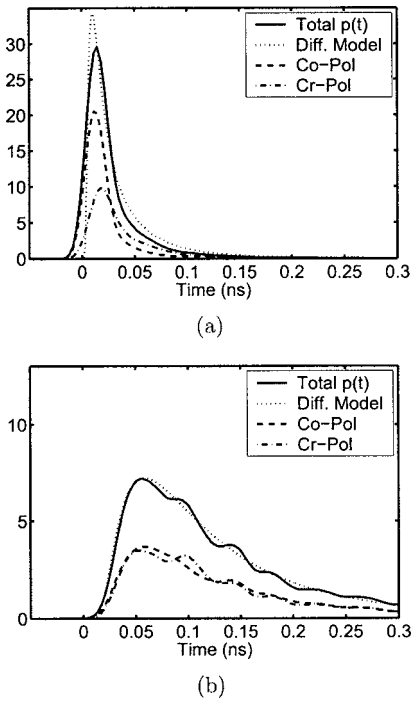

Fig. 8. Ensemble averages of 100 measurements of the temporal response of scattering samples ($\mu_s' = 14\ \mathrm{cm}^{-1}$) of thickness (a) 3 mm and (b) 6 mm for both co-polarized and cross-polarization states and the total response, along with a diffusion model simulation for comparison.

cross-polarized temporal responses, which corresponds to the total temporal response, has an integral of one. This total response can be viewed as the photon time-of-flight distribution.

The measured DOP as a function of sample thickness for the $\mu_s' = 4\ \mathrm{cm}^{-1}$ and $\mu_s' = 14\ \mathrm{cm}^{-1}$ samples is given in Fig. 7. Light in the more strongly scattering sample depolarizes more rapidly with increasing thickness. The results for the more weakly scattering sample suggest the expected range for the DOP: from one at zero thickness and approaching zero as the thickness increases. In the more weakly scattering sample we used, the light is nearly depolarized for thicknesses of approximately 21 mm.

Figure 8 shows the temporal responses extracted from the interferometer data for the material having $\mu_s' = 14\ \mathrm{cm}^{-1}$ and thickness 3 mm [Fig. 8(a)] and 6 mm [Fig. 8(b)]. The co-polarized and cross-polarized responses were scaled to the measured relative energies, consistent with the DOP data of Fig. 7. The total $p(t)$ consequently has an integral of one, which is consistent with its nature as a density function. All responses used an ensemble average of 100 independent measurements. Note that for the 3 mm result, the response is nonzero for $t < 0$, which is a consequence of the finite measurement bandwidth, as expressed in Eq. (14). Figure 7 shows that the 6 mm sample completely depolarizes the input, so the co-polarized and cross-polarized temporal responses are similar, as seen in Fig. 8. Good agreement between the total temporal responses for the samples and diffusion model simulations, which were scaled to be density functions, is evident.

The measured relationship between scattering and DOP in Fig. 7 suggests that (i) for few scattering events, which is equivalent to the early time portion of the temporal response, the co-polarized response should be larger than the cross-polarized response, and (ii) for many scattering events, which is equivalent to the later time portion, the co-polarized and cross-polarized responses should be similar. The 3 mm sample result in Fig. 8 provides evidence from our experimental technique for (i) and (ii). This supports previous experimental evidence

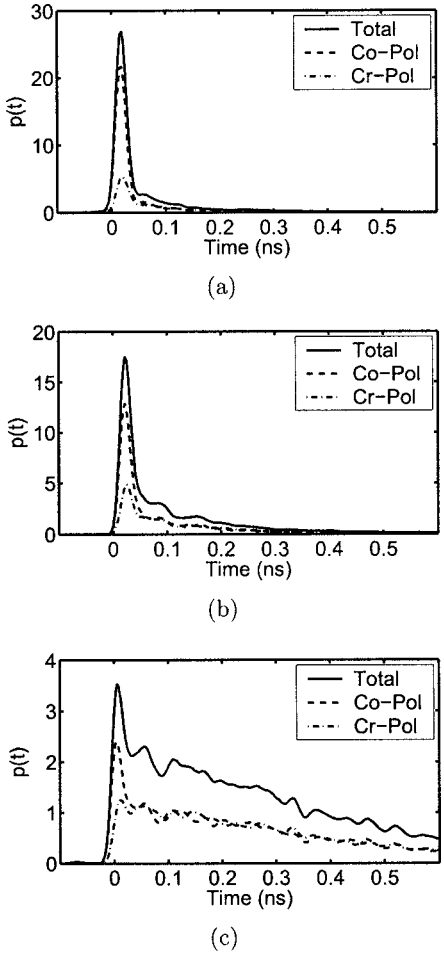

Fig. 9. Total and co- and cross-polarized responses according to sample thickness ($\mu_s' = 4\ \mathrm{cm}^{-1}$): (a) 9 mm, (b) 12 mm, (c) 18 mm.

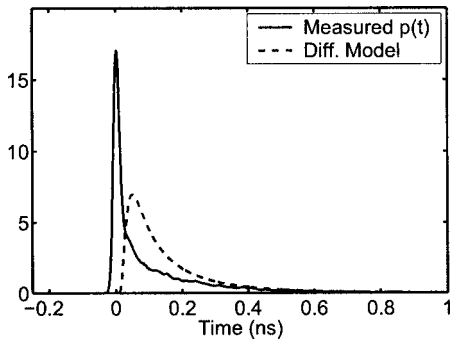

Fig. 10. Total temporal response for 12 mm sample (μ_s' $=4$ cm^{-1}) compared with the diffusion model simulated result.

provided by Wang *et al.*[24] for these two conditions. Figure 9 shows the temporal responses for 9, 12, and 18 mm thick samples having $\mu_s'=4$ cm^{-1}, for both co-polarized and cross-polarization states. Again, the co- and cross-polarized responses are normalized according to the DOP for each sample, and the total response integrates to unity. For early times, the co-polarized and cross-polarized responses are quite different for the three sample thicknesses and in agreement with (i). For later times, the two polarization state responses become approximately equivalent, in agreement with (ii). For these more weakly scattering samples, the early time responses appear quite peaked, and the overall responses do not agree well with results simulated with a diffusion model, as seen in Fig. 10.

Referring to Fig. 7, the 3 mm sample having μ_s' $=14$ cm^{-1} and the 12 mm sample having $\mu_s'=4$ cm^{-1} both have $P\sim 0.2$. One might expect that the temporal responses may be similar, and indeed from Fig. 8(a) and Fig. 9(b), this is the case. Assuming that the scatterers have the same size and shape and a sample thickness d, the number of scattering events is proportional to d/l_s, because of the scattering angle relation between the scattering length (the average distance between scattering events) and l_s. Using this measure, $d/l_s=4.8$ for the 12 mm sample and $d/l_s=4.2$ for the 3 mm sample, supporting the impulse response data similarities. In this scatter regime the diffusion equation does not perform particularly well [there is an $\exp(d^2/l_s)$ dependency in the diffusion model[30]]. However, the diffusion model does appear to perform better for the thinner, higher μ_s' sample [see Fig. 8(a)] than for the thicker, lower μ_s' case (see Fig. 10).

5. CONCLUSION

Spectral interferometry provides access to the field scattered by a random medium. This approach allows polarization-sensitive measurements of scattered field amplitude and phase at optical frequencies with relatively inexpensive and simple equipment. The statistics from such a measurement proved to be circular Gaussian for the frequency scan and samples studied, supporting a key assumption in statistical optics. With linearly polarized input light, the measurements provide co-polarized and cross-polarized temporal responses that could be used to learn more about a scattering medium. The approach can be extended to form a complete polarization state description.

ACKNOWLEDGMENT

This work was supported by the National Science Foundation under contracts 9901907-ECS, 0203240-ECS, and 0323037-ECS.

Corresponding author K. J. Webb can be reached by e-mail at webb@purdue.edu.

REFERENCES

1. A. Ishimaru, *Wave Propagation and Scattering in Random Media* (Academic, 1978).
2. H. T. Shang, "Chromatic dispersion measurement by white-light interferometry on meter-length single-mode optical fibers," Electron. Lett. **17**, 603–605 (1981).
3. D. Huang, E. A. Swanson, C. P. Lin, J. S. Schuman, W. G. Stinson, W. Chang, M. R. Hee, T. Flotte, K. Gregory, and C. A. Puliafito, "Optical coherence tomography," Science **254**, 1178–1181 (1991).
4. W. Drexler, U. Morgner, F. X. Kartner, C. Pitris, S. A. Boppart, X. D. Li, E. P. Ippen, and J. G. Fujimoto, "*In vivo* ultrahigh-resolution optical coherence tomography," Opt. Lett. **24**, 1221–1223 (1999).
5. S. R. Arridge, "Optical tomography in medical imaging," Inverse Probl. **15**, R41–R43 (1999).
6. A. B. Milstein, S. Oh, J. S. Reynolds, K. J. Webb, C. A. Bouman, and R. P. Millane, "Three-dimensional Bayesian optical diffusion tomography with experimental data," Opt. Lett. **27**, 95–97 (2002).
7. A. Labeyrie, "Attainment of diffraction limited resolution in large telescopes by Fourier analysing speckle patterns in star images," Astron. Astrophys. **6**, 85–87 (1970).
8. K. Creath, "Phase-shifting speckle interferometry," Appl. Opt. **24**, 3053–3058 (1985).
9. J. A. Leendertz, "Interferometric displacement measurement on scattering surfaces utilizing speckle effect," J. Phys. E **3**, 214–218 (1970).
10. C. A. Thompson, K. J. Webb, and A. M. Weiner, "Imaging in scattering media by use of laser speckle," J. Opt. Soc. Am. A **14**, 2269–2277 (1997).
11. C. A. Thompson, K. J. Webb, and A. M. Weiner, "Diffusive media characterization with laser speckle," Appl. Opt. **36**, 3726–3734 (1997).
12. J. D. McKinney, M. A. Webster, K. J. Webb, and A. M. Weiner, "Characterization and imaging in optically scattering media by use of laser speckle and a variable-coherence source," Opt. Lett. **25**, 4–6 (2000).
13. M. A. Webster, K. J. Webb, and A. M. Weiner, "Temporal response of a random medium from third order laser speckle frequency correlations," Phys. Rev. Lett. **88**, 033901 (2002).
14. M. A. Webster, K. J. Webb, A. M. Weiner, J. Xu, and H. Cao, "Temporal response of a random medium from speckle intensity frequency correlations," J. Opt. Soc. Am. A **20**, 2057–2070 (2003).
15. J.-M. Tualle, E. Tinet, and S. Avrillier, "A new and easy way to perform time-resolved measurements of the light scattered by a turbid medium," Opt. Commun. **189**, 211–220 (2001).
16. A. A. Chabanov and A. Z. Genack, "Field distributions in the crossover from ballistic to diffusive wave propagation," Phys. Rev. E **56**, R1338–R1341 (1997).
17. P. Sebbah, O. Lengrand, B. A. van Tiggelen, and A. Z. Genack, "Statistics of the cumulative phase of microwave radiation in random media," Phys. Rev. E **56**, 3619–3623 (1997).
18. P. Sebbah, R. Pnini, and A. Z. Genack, "Field and intensity

correlation in random media," Phys. Rev. E **62**, 7348–7352 (2000).
19. J. Pearce, Z. Jian, and D. M. Mittleman, "Statistics of multiply scattered broadband terahertz pulses," Phys. Rev. Lett. **91**, 043903 (2003).
20. J. W. Goodman, "Statistical properties of laser speckle patterns," in *Laser Speckle and Related Phenomena*, 2nd ed., J. C. Dainty, ed. (Springer-Verlag, 1984).
21. M. A. Webster, T. D. Gerke, K. J. Webb, and A. M. Weiner, "Spectral and temporal speckle field measurements of a random medium," Opt. Lett. **29**, 1491–1493 (2004).
22. S. Ito and T. Oguchi, "Approximate solutions of the vector radiative transfer equation for linearly polarized light in discrete random media," J. Opt. Soc. Am. A **6**, 1852–1858 (1989).
23. A. Ishimaru, S. Jaruwatanadilok, and Y. Kuga, "Polarized pulse waves in random discrete scatterers," Appl. Opt. **40**, 5495–5502 (2001).
24. X. Wang, L. V. Wang, C.-W. Sun, and C.-C. Yang, "Polarized light propagation through scattering media: time-resolved Monte Carlo simulations and experiments," J. Biomed. Opt. **8**, 608–617 (2003).
25. L. Lepetit, G. Cheriaux, and M. Joffre, "Linear techniques of phase measurement by femtosecond spectral interferometry for applications in spectroscopy," J. Opt. Soc. Am. B **12**, 2467–2474 (1995).
26. J. J. Duderstadt and L. J. Hamilton, *Nuclear Reactor Analysis* (Wiley, 1976).
27. J. W. Goodman, *Introduction to Fourier Optics*, 2nd ed. (McGraw-Hill, 1996).
28. C.-T. Chen, *Digital Signal Processing: Spectral Computation and Filter Design* (Oxford U. Press, 2001).
29. E. P. Ippen and C. V. Shank, "Techniques for measurement," in *Ultrashort Light Pulses: Picosecond Techniques and Applications*, S. H. Shapiro, ed., (Springer-Verlag, 1984), Vol. 18, pp. 83–122.
30. M. S. Patterson, B. Chance, and B. C. Wilson, "Time resolved reflectance and transmittance for the non-invasive measurement of tissue optical properties," Appl. Opt. **28**, 2331–2336 (1989).